Check for updates

Indium Doping of Lead-Free Perovskite Cs$_2$SnI$_6$

Shodruz T. Umedov[1], Anastasia V. Grigorieva[1,2]*, Leonid S. Lepnev[3],
Alexander V. Knotko[1,2], Koji Nakabayashi[4], Shin-ichi Ohkoshi[4] and Andrei V. Shevelkov[2]

[1] Department of Materials Science, Lomonosov Moscow State University, Moscow, Russia, [2] Department of Chemistry, Lomonosov Moscow State University, Moscow, Russia, [3] Lebedev Physical Institute of the Russian Academy of Sciences, Moscow, Russia, [4] Department of Chemistry, School of Sciences, University of Tokyo, Tokyo, Japan

Structure and properties of an inorganic perovskite Cs$_2$SnI$_6$ demonstrated its potential as a light-harvester or electron-hole transport material; however, its optoelectronic properties are poorer than those of lead-based perovskites. Here, we report the way of light tuning of absorption and transport properties of cesium iodostannate(IV) Cs$_2$SnI$_6$ via partial heterovalent substitution of tin for indium. Light absorption and optical bandgaps of materials have been investigated by UV-vis absorption and photoluminescent spectroscopies. Low-temperature electron paramagnetic resonance spectroscopy was used to study the kind of paramagnetic centers in materials.

Keywords: perovskite photovoltaics, cesium iodostannate(IV), solid solution, Raman spectroscopy, optical characteristics

INTRODUCTION

The efficiency of third-generation solar cells (SCs) based on materials with a perovskite structure is growing every year (Elumalai et al., 2016; Li et al., 2016; Powalla et al., 2018; Sani et al., 2018; Ajay et al., 2019). Such rapid success of using these materials in various fields of solar photovoltaics is due to their unique optoelectronic properties. Today, lead-based perovskite materials (APbX$_3$) are the most efficient in terms of converting solar radiation into electricity (Brandt et al., 2015; Dimesso et al., 2017; Yang et al., 2017; Zhu Z. et al., 2019), and it is caused by low binding energy of excitons, charge carrier mobility, long diffusion length, high absorption coefficient, and direct bandgap (Xiao and Yan, 2017; Deng et al., 2019). The theoretically calculated highest power conversion efficiency (PCE) (Shockley–Queisser limit) achieved by lead-based perovskite is 31.4% for CH$_3$NH$_3$PbI$_3$ (Wan-Jian et al., 2015) and the experimental efficiency (light converting efficiency) of SCs with this compound has exceeded 25% (Yang et al., 2017; Jeon et al., 2018; Powalla et al., 2018). However, the chemical and thermal stability of lead perovskites are not sufficiently well; moreover, lead is a toxic element (Kulbak et al., 2016; Wu Y. et al., 2017; Pisanu et al., 2019). These problems motivate finding new alternatives among lead-free materials with optimal optoelectronic characteristics (Hoefler et al., 2017; Fu, 2019; Pisanu et al., 2019). Instead of lead perovskites, materials with general formulas of ABX$_3$ [where A = CH$_3$NH$_3^+$, HC(NH$_2$)$_2^+$, or Cs$^+$, Rb$^+$, K$^+$; B = divalent inorganic cation; X = Cl, Br, I] and A$_2$BX$_6$ (where A and X the same cations and anions as in the case of ABX$_3$; B = tetravalent inorganic cations) are in focus for investigations (Huang and Lambrecht, 2013; Stoumpos et al., 2016; Cai et al., 2017; Ju et al., 2017). Among all lead-free compounds with the ABX$_3$ formula, cesium triiodostannate CsSnI$_3$ turned out to be the most promising material with good optoelectronic performance (Kumar et al., 2014, 2017; da Silva et al., 2015; Stoumpos et al., 2016). The first SCs based on Sn^{2+} perovskites had a very low efficiency (3 × 10^{-4}%−2%) (Chen et al., 2012; Kumar et al., 2014). Nevertheless, CsSnI$_3$ has excellent properties [optimal

bandgap of 1.4 eV, higher theoretical short-circuit photocurrent (J_{SC}) density of 34.3 mA cm^{-2}, highest hole mobility ~585 cm^2 V^{-1} s^{-1} among p-type materials] for photovoltaic application as light harvesting or p-type semiconductor (Chung et al., 2012; Stoumpos et al., 2013). Thereby, the CsSnI$_3$ phase is still being actively studied (Song et al., 2018; Wijesekara et al., 2018; Pisanu et al., 2019) and the PCE of SCs based on it has achieved 5.03% (Wang Y. et al., 2019), but these results are still less satisfactory than those of MAPbI$_3$.

Another type of compounds are double perovskites, which are obtained by replacing the tetravalent cation B^{4+} and a vacancy in A$_2$BX$_6$ with the B$^+$/B^{3+} pair (where B$^+$ = Cu, Ag, Ga, In, Tl, etc.; B^{3+} = Sb, Bi etc.) so that the charge neutrality is preserved (Yin et al., 2019). According to Savory et al. (2016), the theoretical calculations show a PCE limit <8% for the double perovskite compound Cs$_2$AgBiX$_6$; however, higher PCE and suitable bandgaps have been predicted for other materials such as Cs$_2$InSbCl$_6$, Cs$_2$AgInBr$_6$, Rb$_2$AgInBr$_6$, and Rb$_2$CuInCl$_6$ (Zhao et al., 2017a,b). According to Xiao et al. (2019), the most promising double perovskites are based on cations such as Ag, In, Bi, and Sb (Greul et al., 2017; Wu C. et al., 2017; Gao et al., 2018; Liang and Gao, 2018; Fan et al., 2019; Igbari et al., 2019).

A promising lead-free non-toxic and stable perovskite-like material with a face-centered cubic cell is A$_2$SnX$_6$, where the tin atom is strongly covalently bonded and stabilizes the crystal lattice. Among all compounds in the A$_2$SnX$_6$ group, the Cs$_2$SnI$_6$ phase turned out to be a suitable material for photovoltaics (Cai et al., 2017; Maughan et al., 2018). Cesium iodostannate(IV) has promising optoelectronic properties (electron mobility up to 509 cm^2 V^{-1} s^{-1}; Guo et al., 2017; J_{SC} = 13.97 mA cm^{-2}; V_{OC} = 0.58 V; E_g = ~1.2 eV) (Kaltzoglou et al., 2016), which makes it a candidate as a light-harvesting material in SCs. Mixed cations A$^+$((A$_x$A$_{1-x}$)$_2$BX$_6$) (Ganesan et al., 2019) and anions X$^-$(A$_2$B(X'$_x$X$_{1-x}$)$_6$) (Lee et al., 2017; Ke et al., 2018; Yuan et al., 2019; Zhu W. et al., 2019) were considered to improve stability and properties of Cs$_2$SnX$_6$. Upon replacement of Cl$^-$ by I$^-$, the optical absorption coefficient increases, the bandgap decreases, stability decreases, and the materials color changes from pale yellow (or white) to black. The Cs$_2$SnI$_6$ phase is also used as photodetectors (Han et al., 2019), for photoelectrochemical water splitting (Dang et al., 2019), as photocatalysts (Wang X.-D. et al., 2019), and the efficiency of the SCs based on it has reached ~11.2%. In this work, we have demonstrated the preparation of solid solutions based on Cs$_2$SnI$_6$ by doping with indium. Heterovalent substitution of tin (Sn^{4+} ionic radii 0.69 Å, Pauling electronegativity = 1.96) in the structure of Cs$_2$SnI$_6$ by indium (In^{3+} ionic radii 0.74 Å, Pauling electronegativity = 1.78) leads to the formation of solid solutions with improved optical properties. Here, for the In^{3+} → Sn^{4+} substitution, the difference in electronegativities of cations is 0.18 and the difference in ion sizes is 7.24%, which corresponds well to the Goldschmidt rule (Goldschmidt, 1926).

Recently, the new wave of enthusiasm among researchers has arrived from coming perspectives of nanocrystalline Cs$_2$SnI$_6$ phase and its derivatives for optoelectronics (Wang et al., 2016; Veronese et al., 2020). Because of this, development of nanochemistry of complex halides requires preliminary fundamental studies of phase equilibrium and analysis of optical and transport characteristics in polycrystalline materials.

EXPERIMENTAL SECTION

Syntheses of Materials

The sintering was carried out by solid-state sintering method in evacuated quartz ampules (RT pressure of 1.6 · 10^{-2} Torr). The compositions were prepared by grinding cesium iodide CsI (Sigma-Aldrich 99.99%), tin iodide SnI$_4$ [direct synthesis from elementary tin ("Ruschim," 99.90+, O-1) and iodine in CCl$_4$ (purum, "Irea2000") with further purification by sublimation at 270°C], and elementary iodine (purum, "Reachim") and metallic indium ("Ruschim," 99.999%) with the stoichiometric mass ratios. The pristine Cs$_2$SnI$_6$ phase was obtained with the stoichiometric mass of CsI and SnI$_4$ (2:1). The mixtures were sealed in preliminarily dried quartz ampules and heated with the rate of ~0.2°C/min to 300°C and then annealed at this temperature for 48 h. All samples were kept in double closed zip-lock bags in nitrogen.

All materials were characterized with powder XRD method for phase composition definition. We assumed that the obtaining materials have the composition related to the solid solutions Cs$_{2-x}$Sn$_{1-x}$In$_x$I$_{6-2x}$ based on Cs$_2$SnI$_6$ or CsInI$_4$ phases. The following chemical equation shows the phase composition and yield of the reaction products.

$$(2-x)CsI + (1-x)SnI_4 + (x)In + (1.5x)I_2 \rightarrow Cs_{2-x}Sn_{1-x}In_xI_{6-2x} \qquad (1)$$

Characterization Methods

The ampules with samples were open right before the following analyses. The samples were transferred to the closely packed cells for further storing. XRD, Raman, and UV-vis measurements were performed in air for 15 min.

X-ray diffraction measurements (XRD) were performed on a Rigaku D/MAX 2500 diffractometer equipped with a rotating copper anode (Cu-Kα radiation) and operated at 45 kV and 250 mA from 5° to 80° in 2Θ; at the continuous scanning speed 5° min^{-1} with a measuring step of 0.02°. The experimental data were analyzed using WinXPow (database PDF2) to define the phase composition, and Jana2006 software was used for unit cell parameter calculations.

To analyze the optical properties, the samples were studied by diffuse reflection spectroscopy. One gram of each compound was placed in the cell of the spectrophotometer and pressed tightly with a quartz glass and then measured in the range of 1,400–200 nm with a scan step of 1 nm. UV-vis diffuse reflectance spectra were collected using a UV-vis spectrometer Lambda 950 (PerkinElmer). All measurements were performed at 298 K with a scanning rate of 2 nm/s using quartz glass as a reference. Reflectance (R) was converted to absorption (α) data in accordance with the Kubelka–Munk model: $\alpha/S = (1 − R)^2/(2·R)$. The optical energy bandgap (E_g) was acquired using a Tauc plot, the dependence of $(\alpha h\nu)^2$ on energy ($h\nu$).
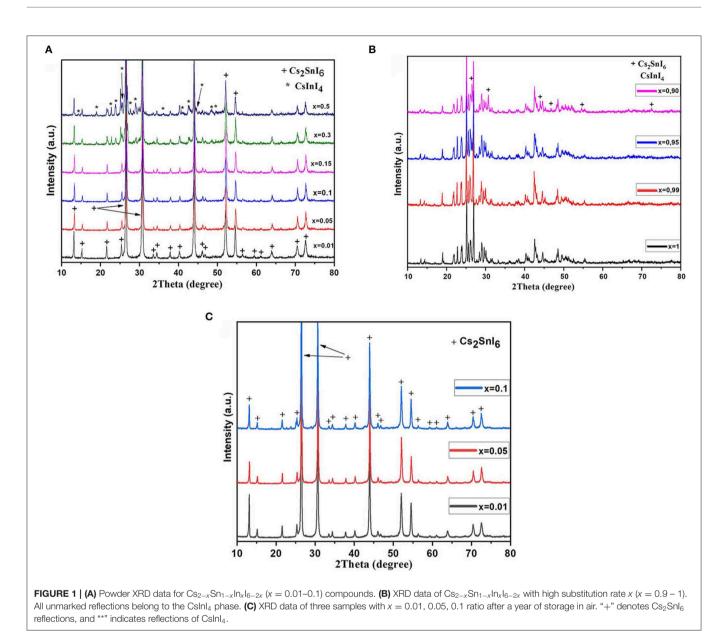
FIGURE 1 | (A) Powder XRD data for Cs$_{2-x}$Sn$_{1-x}$In$_x$I$_{6-2x}$ ($x = 0.01$–0.1) compounds. **(B)** XRD data of Cs$_{2-x}$Sn$_{1-x}$In$_x$I$_{6-2x}$ with high substitution rate x ($x = 0.9 - 1$). All unmarked reflections belong to the CsInI$_4$ phase. **(C)** XRD data of three samples with $x = 0.01$, 0.05, 0.1 ratio after a year of storage in air. "+" denotes Cs$_2$SnI$_6$ reflections, and "*" indicates reflections of CsInI$_4$.

TABLE 1 | XRD data for Cs$_{2-x}$Sn$_{1-x}$In$_x$I$_{6-2x}$ compositions.

Sample composition	Substitution rate x	Cell parameter a, Å	Unit cell volume V, Å^3	R_p	R_l
Cs$_{1.99}$Sn$_{0.99}$In$_{0.01}$I$_{5.98}$	0.01	11.6505 (6)	1581.4 (1)	13.66	5.52
Cs$_{1.95}$Sn$_{0.95}$In$_{0.05}$I$_{5.9}$	0.05	11.6541 (6)	1582.8 (1)	14.34	5.80
Cs$_{1.9}$Sn$_{0.9}$In$_{0.1}$I$_{5.8}$	0.10	11.6548 (3)	1583.1 (1)	15.91	6.32

Emission spectra were collected with a multichannel spectrometer S2000 (Ocean Optics) with a nitrogen LGI-21 ($\lambda_{ex} = 337$ nm) as an excitation source at 293 K and 77 K. All spectra were corrected for the wavelength response of the system. Additionally, the photoluminescence emission spectra of the sample CsInI$_4$ was investigated with a diode source of 365 nm.

EPR spectra were recorded using a X-band JES-FA200 (JEOL) spectrometer at the temperature of 294–4.2 K. The modulation frequency is 100 kHz and microwave frequencies are around 9.00

GHz. The samples are put in a quartz tube with an upper glass part, then purged by Ar gas and vacuum three times, and finally sealed in vacuum (about 20 Pa).

RESULTS AND DISCUSSION

As shown in **Figure 1A**, about 10% of tin atoms in the structure of Cs$_2$SnI$_6$ can be substituted by indium atoms. All reflections on the corresponding XRD patterns belong to the Cs$_2$SnI$_6$

with a cubic structure and space group $Fm\text{-}3m$(225) (PDF2 file #73-330). Diffraction patterns for the compositions with x from 0 to 0.15 display a shift of the reflections toward lower 2θ upon increasing the substitution rate. The increase of the unit cell parameter a compared to pure Cs_2SnI_6 phase indicates a slight increase of the unit cell volume. According to the fact that the ionic radius of the In^{3+} (0.74 Å) is slightly larger than that of Sn^{4+} (0.69 Å), the cell volume increases. At higher substitution rates, x of 0.3 and 0.5, reflections of the $CsInI_4$ phase (PDF2 file #76-2101) with a monoclinic structure [$P21/c$ (14) space group] are observed on diffraction patterns of the respective samples. The estimated cell parameters of the F-centered cubic Cs_2SnI_6 are given
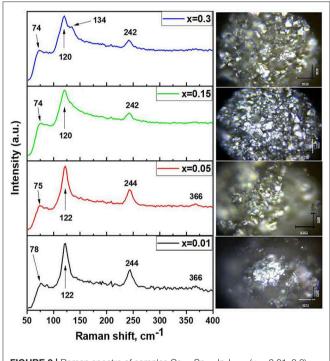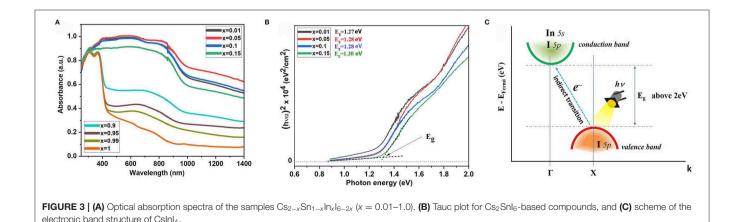

FIGURE 2 | Raman spectra of samples $Cs_{2-x}Sn_{1-x}In_xI_{6-2x}$ ($x = 0.01–0.3$) and their optical microscopy data.
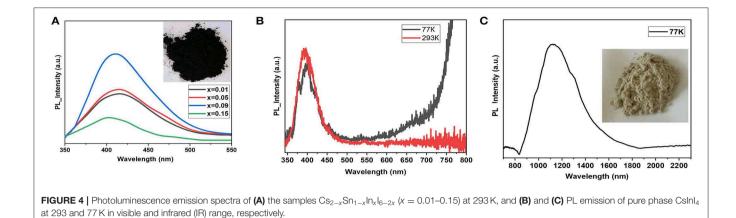
in **Table 1**. Such gentle change of the unit cell parameters is probably due to the formation of iodine vacancies in the anion sublattice.

Samples (polycrystalline powders) were stored in air under laboratory conditions for 1 year and investigated by powder XRD repeatedly during this period. According to the XRD results (**Figure 1**), the indium-substituted samples remain single-phase with the cubic Cs_2SnI_6 structure, while the pristine Cs_2SnI_6 phase (without doping) decomposed already after a month of storage into CsI and volatile SnI_4, which turned into SnO_2 as a result of hydrolysis. The stability of the substituted samples is probably due to the fact that indium with iodine form stronger ionic bonds than tin; therefore, the lattice of solid solutions is more stable than the pure phase lattice. At the same time, the sample with $x = 0.10$ has very weak reflections of admixture at 18.77°, 22.65°, and 23.66° in this XRD pattern. These reflections most probably belong to the $CsInI_4$ phase. For comparison, the strongest reflections of cesium iodide CsI should be at 22.87°, 32.56°, and 52.63°. The impurity is probably a result of the segregation process.

The samples of In-substituted Cs_2SnI_6 were studied by Raman spectroscopy. As can be seen from optical microscopy (**Figure 2**), the samples are homogeneous in appearance and all crystallites have a similar color. The spectra contain the strongest modes $\nu(A_{1g})$—122 cm^{-1}, $\nu(E_g)$—83 cm^{-1}, and $\delta(F_{2g})$—78 cm^{-1}, which are related to vibrations of $[SnI_6]^{2-}$ octahedra [namely, $\nu(A_{1g})$ is a symmetric stretching of Sn–X bonds; $\delta(F_{2g})$ is a X–Sn–X asymmetric bending]. Substitution of Sn^{4+} with In^{3+} resulted in shortening of M–I bonds and distortion of $[MI_6]^{2-}$ octahedrons. Since Cs_2SnI_6 perfectly absorbs the visible part of the spectrum, the excitation by a green laser (wavelength, 514.4 nm) excites second- and third-order harmonics at 244 and 366 cm^{-1} due to strong resonance. The relative shift of the lines relative to the theoretical ones in the direction of smaller or larger wave numbers is associated with a changing energy and lengths of the Sn–I bonds in the $[SnI_6]^{2-}$ octahedra. Substitution of tin by indium results in small "left shift" and broadening of $\nu(A_{1g})$, and $\delta(F_{2g})$ Raman modes show the increase of element–iodine bond length. Raman spectra of the In-doped Cs_2SnI_6 differ

FIGURE 3 | (A) Optical absorption spectra of the samples $Cs_{2-x}Sn_{1-x}In_xI_{6-2x}$ ($x = 0.01–1.0$). **(B)** Tauc plot for Cs_2SnI_6-based compounds, and **(C)** scheme of the electronic band structure of $CsInI_4$.

FIGURE 4 | Photoluminescence emission spectra of **(A)** the samples $Cs_{2-x}Sn_{1-x}In_xI_{6-2x}$ ($x = 0.01$–0.15) at 293 K, and **(B)** and **(C)** PL emission of pure phase $CsInI_4$ at 293 and 77 K in visible and infrared (IR) range, respectively.

also from the spectrum reported by Qui et al. for pure Cs_2SnI_6 (Qiu et al., 2017).

In the Raman spectrum of the two-phase sample $x = 0.3$, a band observed at 134 cm^{-1} corresponds to the vibration of the $[InI_4]^-$ tetrahedron. Namely, $\nu(A_{1g})$ is a symmetric stretching vibration of In–I bonds in $[InI_4]^-$ tetrahedral in $CsInI_4$ phase. Other vibration modes of $[InI_4]^-$ tetrahedra do not appear in the spectra. It was found that Raman spectrum of the $x = 0.15$ sample had an additional shoulder at 134 cm^{-1}. The possible reason for this is a fine and evenly distributed admixture of $CsInI_4$. Its XRD reflections do not present in diffractograms, but Raman spectroscopy revealed its presence as the surface admixture. Eventually, this admixture recrystallizes, leading to larger crystallites of cesium iodogallate.

The optical absorption spectra shown in **Figure 3** consist of two maxima (at ~800 nm and at ~600 nm). The materials absorb from the near infrared (from 1,000 nm) to ultraviolet (UV) (380 nm). The first local maximum (~800 nm) is due to the transition of the electrons from the maximum of valence band (which is formed from I $5p$ orbitals) to the minimum of conduction band formed by hybridized I $5p$–Sn $5s$ orbitals. This transition is characteristic for all the samples excluding $x = 1$. The estimated bandgap energy grows slightly from 1.27 to 1.31 eV for the single-phase samples with $x = 0$–0.15 according to the corresponding Tauc plots (**Figure 3B**). The second peak in energy is approximately equal to the electron transfer energy from slightly hybridized I $5p$–Sn $5p$ orbitals localized below the top of the valence band to hybridized I $5p$–Sn $5s$ orbitals of the conduction band.
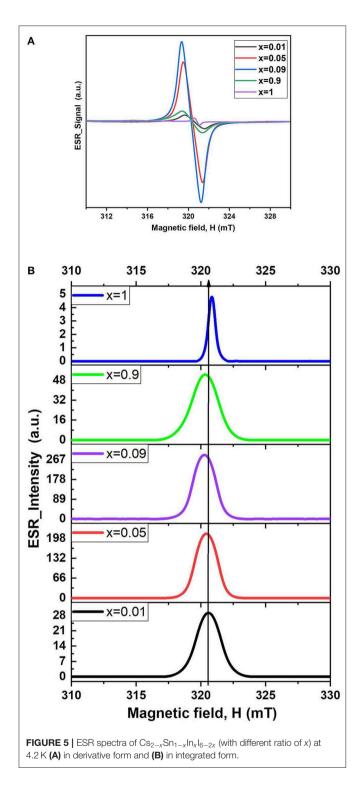
As the indium concentration in the composition of the materials increases, the content of the $CsInI_4$ phase increases, as can be seen from the XRD data, and this is manifested in the absorption spectrum of the sample $x = 0.5$ (~370 nm). This absorption edge is approximately equal to ~3.0 eV and relates to transitions in the electronic structure of the $CsInI_4$ phase (**Figure 3B**), namely, the electron transition from the I $5p$ orbitals (top valence band) to the hybridized I $5p$–In $5s$ orbitals (conduction band bottom). The experimental E_g differs from the calculated bandgap value presented in Persson (2016).

Figure 4A shows photoluminescence spectra of the samples. The C_2SnI_6 perovskite phase demonstrates rather moderate intensity of luminescence with the 337-nm (3.68 eV) excitation laser, while its In-doped analog shows an intensive violet band at 410 ± 10 nm. Its intensity increases with an increase in the doping level x. Weaker broad maxima in 450–480 nm regions are observed for the samples with lower substitution rate.

Most likely, the PL of the solid solutions $Cs_{2-x}Sn_{1-x}In_xI_{6-2x}$ ($x = [0; 0.1]$) corresponds to cascade relaxation of electrons from the high free levels (anti-bonding derivative of Sn5p^0 orbital) to the valence band (Xiao et al., 2015). It has been demonstrated that decrease of the temperature up to 77 K leads to devolution of the PL process. Such behavior is typical for materials with a gap slightly larger than the excitation laser wavelength. The visible photoluminescence in Cs_2SnI_6 phase is observed as a result of complex relaxation processes. The relaxation of the excited electron to the bottom of the conduction band occurs with visible luminescent process, and the following transition to the top of the valence band has a much lower energy than the observed PL process. Participation of deep levels originated from the point defects (V_I) and is another possible reason for the PL effect in the visible diapason (Maughan et al., 2018).

For comparison, the gray cesium iodoindate(III) shows intensive PL bands at 380 ± 10 nm and 400 ± 10 nm in the visible region and intensive PL process in IR diapason at 1,170 ± 20 nm (1.16 eV) (**Figures 4B,C**). The 380-nm (3.26 eV) band correlates with the experimental band gap transition above while the second maximum in the visible range probably corresponds to shallow defects or self-trapped exciton processes. Intensive IR photoluminescence also originates from self-defect in cesium iodoindate, but the deep level is attributed to deficiency in iodine sublattice.

It is remarkable that the electron spin resonance effect is more significant for the cesium iodostannate(IV) phase with doped indium than for the pure phase. The ESR spectra for the $Cs_{2-x}Sn_{1-x}In_xI_{6-2x}$ ($x = 0.01, 0.05, 0.09, 0.9,$ and 1) shown

FIGURE 5 | ESR spectra of $Cs_{2-x}Sn_{1-x}In_xI_{6-2x}$ (with different ratio of x) at 4.2 K **(A)** in derivative form and **(B)** in integrated form.

TABLE 2 | ESR spectra characteristics.

Sample composition	Substitution rate x	Integration curve area	g-factor
$Cs_{1.99}Sn_{0.99}In_{0.01}I_{5.98}$	0.01	68.6	2.0045
$Cs_{1.95}Sn_{0.95}In_{0.05}I_{5.9}$	0.05	440.4	2.0051
$Cs_{1.9}Sn_{0.9}In_{0.1}I_{5.8}$	0.09	604.9	2.0054
$Cs_{1.1}Sn_{0.1}In_{0.9}I_{4.2}$	0.9	134	2.0065
$CsInI_4$	1	3.4	2.0029

substitution level x in the solid solution (**Table 2**), suggesting increment of the defects. The values of the g-factors and the areas calculated by the integration are given in **Table 2**. The spectra of the two-phase composition with x of 0.9 include less intensive and broad maximum at 321.2 mT. Probably, there could be an input shoulder related to the tin-doped cesium tetraiodoindate phase while the largest maximum corresponds to the spectrum of the solid solution $Cs_{2-x}Sn_{1-x}In_xI_{6-2x}$ saturated by In^{3+}. Lower ESR resonance in $CsInI_4$ phase, likely, attributed to lower defect concentration in cesium tetraiodoindate as a result of tetrahedral environment of indium and lower doping level.

CONCLUSIONS

The perovskite-like phase Cs_2SnI_6 forms substitution solid solutions, changing tin to indium, forming a substitution solid solution of about 10 at.% of dopant. Increase of the indium percentage leads to growth of ESR and photoluminescence effects for the material. The successful experience in heterovalent substitution of tin(IV) with elementary indium and iodine as precursors opens new challenges for "improving" the characteristics of cesium iodostannate for its application in photovoltaics or optoelectronic devices. Weak degradation of doped phase in comparison to pure Cs_2SnI_6 is a strong advantage of the new investigated materials. Analysis of optical properties has shown an increase of absorption coefficient of the material that originated from growth of occupancy in the valence band. The intensity of blue photoluminescence also grows with a substitution rate up to 15%.

DATA AVAILABILITY STATEMENT

All datasets generated for this study are included in the article/supplementary material.

AUTHOR CONTRIBUTIONS

SU: synthesis of the samples, Raman spectroscopy experiments and discussion, optical spectroscopy and discussion, ESR experiments. AG: PL spectroscopy and ESR spectroscopy data discussion, correction of the text, and funding. LL: PL spectroscopy experiments. AK: XRD measurements and discussion. KN: ESR experiments and correction of the text. SO:

in **Figure 5** demonstrate week shift of the resonance towards lower field values by the doping of indium from $x = 0.01$ to $x = 0.9$, resulting in the shift of the g-factor from 2.0045 to 2.0065. In the range of $x = 0.01$ to $x = 0.09$, the integral intensity of the ESR spectra grows up with increase of the

ESR experiment discussion. AS: XRD discussion and correction of the text.

FUNDING

This project has been performed using the equipment and setups of the collective resource center of Moscow State University Technologies for synthesis of new nanostructured materials and their complex characterization. The reported study was funded

by the Russian Foundation for Basic Research according to the research project N 19-03-00849_a.

ACKNOWLEDGMENTS

The authors are grateful to colleagues Dr. Tatyana A. Shestimerova, and Dr. Valery Yu. Verchenko (Lomonosov Moscow State University) for their assistance in XRD experiments.

REFERENCES

Ajay, K. J., Ashish, K., and Tsutomu, M. (2019). Halide perovskite photovoltaics: background, status, and future prospects. *Chem. Rev.* 119, 3036–3103. doi: 10.1021/acs.chemrev.8b00539

Brandt, R. E., Stevanović, V., Ginley, D. S., and Buonassisi, T. (2015). Identifying defect-tolerant semiconductors with high minority-carrier lifetimes: beyond hybrid lead halide perovskites. *MRS Commun.* 5, 265–275. doi: 10.1557/mrc.2015.26

Cai, Y., Xie, W., Ding, H., Chen, Y., Thirumal, K., Wong, L. H., et al. (2017). Computational study of halide perovskite-derived A_2BX_6 inorganic compounds: chemical trends in electronic structure and structural stability. *Chem. Mater.* 29, 7740–7749. doi: 10.1021/acs.chemmater.7b02013

Chen, Z., Wang, J. J., Ren, Y., Yu, C., and Shum, K. (2012). Schottky solar cells based on $CsSnI_3$ thin-films. *Appl. Phys. Lett.* 101:093901. doi: 10.1063/1.4748888

Chung, I., Song, J. H., Im, J., Androulakis, J., Malliakas, C. D., Li, H., et al. (2012). $CsSnI_3$: semiconductor or metal? High electrical conductivity and strong near-infrared photoluminescence from a single material. High hole mobility and phase-transitions. *J. Am. Chem. Soc.* 134, 8579–8587. doi: 10.1021/ja301539s

da Silva, E. L., Skelton, J. M., Parker, S. C., and Walsh, A. (2015). Phase stability and transformations in the halide perovskite $CsSnI_3$. *Phys. Rev. B* 91:144107. doi: 10.1103/PhysRevB.91.144107

Dang, T. C., Le, H. C., Pham, D. L., Nguyen, S. H., Nguyen, T. T. O., Nguyen, T. T., et al. (2019). Synthesis of perovskite Cs_2SnI_6 film via the solution processed approach: first study on the photoelectrochemical water splitting application. *J. Alloys Compd.* 805, 847–851. doi: 10.1016/j.jallcom.2019. 07.122

Deng, J., Li, J., Yang, Z., and Wang, M. (2019). All-inorganic lead halide perovskites: a promising choice for photovoltaics and detectors. *J. Mater. Chem. C* 7, 12415–12440. doi: 10.1039/C9TC04164H

Dimesso, L., Das, C., Stöhr, M., and Jaegermann, W. (2017). Investigation of cesium tin/lead iodide ($CsSn_{1-x}Pb_xI_3$) systems. *Mater. Res. Bull.* 85, 80–89. doi: 10.1016/j.materresbull.2016.08.052

Elumalai, N. K., Mahmud, M. A., Wang, D., and Uddin, A. (2016). Perovskite solar cells: progress and advancements. *Energies* 861, 1–20. doi: 10.3390/en9110861

Fan, Q., McGee, G. V. B., Ma, J., Xu, Q., Pan, S., Peng, J., et al. (2019). Lead-free halide perovskite nanocrystals: crystal structures, synthesis, stabilities, and optical properties. *Angew. Chem. Int. Ed.* 59, 1030–1046. doi: 10.1002/anie.201904862

Fu, H. (2019). Review of lead-free halide perovskites as light-absorbers for photovoltaic applications: from materials to solar cells. *Solar Energy Mater. Solar Cells* 193, 107–132. doi: 10.1016/j.solmat.2018.12.038

Ganesan, R., Vinodhini, S. P., Balasubramani, V., Parthipan, G., Sridhar, T. M., Arulmozhi, M., et al. (2019). Tuning the band gap of hybrid lead free defect perovskite nano crystals for solar cell applications. *New J. Chem.* 43, 15258–15266. doi: 10.1039/C9NJ03902C

Gao, W., Ran, C., Xi, J., Jiao, B., Zhang, W., Wu, M., et al. (2018). High-quality Cs2AgBiBr6 double perovskite film for lead-free inverted planar heterojunction solar cells with 2.2 % efficiency. *ChemPhysChem* 19, 1696–1700. doi: 10.1002/cphc.201800346

Goldschmidt, V. M. (1926). Die Gesetze der Krystallochemie. *Naturwissenschaften* 14, 477–485.

Greul, E., Petrus, M. L., Binek, A., Docampo, P., and Bein, T. (2017). Highly stable, phase pure Cs2AgBiBr6 double perovskite thin films for optoelectronic applications. *J. Mater. Chem. A* 37, 5, 19972–19981. doi: 10.1039/C7TA06816F

Guo, F., Lu, Z., Mohanty, D., Wang, T., Bhat, I. B., Zhang, S., et al. (2017). A two-step dry process for Cs_2SnI_6 perovskite thin film. *Mater. Res. Lett.* 5, 540–546. doi: 10.1080/21663831.2017.1346525

Han, X., Liang, J., Yang, J.-H., Soni, K., Fang, Q., Wang, W., et al. (2019). Lead-free double perovskite Cs_2SnX_6: facile solution synthesis and excellent stability. *Small* 15:1901650. doi: 10.1002/smll.2019 01650

Hoefler, S. F., Trimmel, G., and Rath, T. (2017). Progress on lead-free metal halide perovskites for photovoltaic applications: a review. *Monatsh. Chem.* Chem. 2017, 148, 795–826. doi: 10.1007/s00706-017-1933-9

Huang, L.-,y., and Lambrecht, W. R. L. (2013). Electronic band structure, phonons, and exciton binding energies of halide perovskites $CsSnCl_3$, $CsSnBr_3$, and $CsSnI_3$. *Phys. Rev. B* 88:165203. doi: 10.1103/PhysRevB.88.165203

Igbari, F., Wang, Z.-K., and Liao, L.-S. (2019). Progress of lead-free halide double perovskites. *Adv. Energy Mater.* 9:1803150. doi: 10.1002/aenm.201803150

Jeon, N. J., Na, H., Jung, E. H., Yang, T.-Y., Lee, Y. G., Kim, G., et al. (2018). A fluorene-terminated hole-transporting material for highly efficient and stable perovskite solar cells. *Nat. Energy* 3, 682–689. doi: 10.1038/s41560-018-0200-6

Ju, M.-G., Chen, M., Zhou, Y., Garces, H. F., Dai, J., Ma, L., et al. (2017). Earth-abundant nontoxic titanium(IV)-based vacancy-ordered double perovskite halides with tunable 1.0 to 1.8 eV bandgaps for photovoltaic applications. *ACS Energy Lett.* 3, 297–304. doi: 10.1021/acsenergylett.7b01167

Kaltzoglou, A., Perganti, D., Antoniadou, M., Kontos, A. G., and Falaras, P. (2016). Stress tests on dye-sensitized solar cells with the Cs_2SnI_6 defect perovskite as hole-transporting material. *Energy Procedia* 102, 49–55. doi: 10.1016/j.egypro.2016.11.317

Ke, J. C.-R., Lewis, D. J., Walton, A. S., Spencer, B. F., O'Brien, P., Thomas, A. G., et al. (2018). Ambient-air-stable inorganic Cs_2SnI_6 double perovskite thin films via aerosol-assisted chemical vapour deposition. *J. Mater. Chem. A* 6, 11205–11214. doi: 10.1039/C8TA03133A

Kulbak, M., Gupta, S., Kedem, N., Levine, I., Bendikov, T., Hodes, G., et al. (2016). Cesium enhances long-term stability of lead bromide perovskite-based solar cells. *J. Phys. Chem. Lett.* 7, 167–172. doi: 10.1021/acs.jpclett.5b02597

Kumar, G. R., Kim, H.-J., Karupannan, S., and Prabhakar, K. (2017). Interplay between Iodide and tin vacancies in $CsSnI_3$ perovskite solar cells. *J. Phys. Chem. C* 121, 16447–16453. doi: 10.1021/acs.jpcc.7b06278

Kumar, M. H., Dharani, S., Leong, W. L., Boix, P. P., Prabhakar, R. R., Baikie, T., et al. (2014). Lead-free halide perovskite solar cells with high photocurrents realized through vacancy modulation. *Adv. Mater.* 26, 7122–7127. doi: 10.1002/adma.201401991

Lee, B., Krenselewski, A., Baik, S. I., Seidman, D. N., and Chang, R. P. H. (2017). Solution processing of air-stable molecular semiconducting iodosalts, $Cs_2SnI_{6-x}Br_x$, for potential solar cell applications. *Sustain. Energy Fuels* 1, 710–724. doi: 10.1039/C7SE00100B

Li, M. H., Yum, J. H., Moon, S. J., and Chen, P. (2016). Inorganic p-type semiconductors: their applications and progress in dye-sensitized solar cells and perovskite solar cells. *Energies.* 9:331. doi: 10.3390/en9050331

Liang, L., and Gao, P. (2018). Lead-free hybrid perovskite absorbers for viable application: can we eat the cake and have it too? *Adv. Sci.* 5:1700331. doi: 10.1002/advs.201700331

Maughan, A. E., Ganose, A. M., Almaker, M. A., Scanlon, D. O., and Neilson, J. R. (2018). Tolerance factor and cooperative tilting effects in vacancy-ordered double perovskite halides. *Chem. Mater.* 30, 3909–3919. doi: 10.1021/acs.chemmater.8b01549

Persson, K. (2016). *Materials Data on CsInI4 (SG:14) by Materials Project*. Berkeley, CA, 7. doi: 10.17188/1277593

Pisanu, A., Speltini, A., Quadrelli, P., Drera, G., Sangaletti, L., and Malavasi, L. (2019) Enhanced air-stability of Sn-based hybrid perovskites induced by dimethylammonium (DMA): synthesis, characterization, aging and hydrogen photogeneration of the MA$_{1--x}$DMA$_x$SnBr$_3$ system. *J. Mater. Chem. C* 7, 7020–7026. doi: 10.1039/C9TC01743G

Powalla, M., Paetel, S., Ahlswede, E., Wuerz, R., Wasserdorf, C. D., and Friedlmeier, T. M. (2018). Thin film solar cells exceeding 22% solar cell efficiency: an overview on CdTe$^-$, Cu(In,Ga)Se^{2-}, and perovskite-based materials. *Appl. Phys. Rev.* 5:041602. doi: 10.1063/1.5061809

Qiu, X., Cao, B., Yuan, S., Chen, X., Qiu, Z., Jiang, Y., et al. (2017). From unstable CsSnI$_3$ to air-stable Cs$_2$SnI$_6$: A lead-free perovskite solar cell light absorber with bandgap of 1.48eV and high absorption coefficient. *Solar Energy Mater. Solar Cells* 159, 227–234. doi: 10.1016/j.solmat.2016.09.022

Sani, F., Shafie, S., Lim, H., and Musa, A. (2018). Advancement on lead-free organic-inorganic halide perovskite solar cells: a review. *Materials* 11:E1008. doi: 10.3390/ma11061008

Savory, C. N., Walsh, A., and Scanlon, D. O. (2016). Can Pb-free halide double perovskites support high-efficiency solar cells? *ACS Energy Lett.* 1, 949–955. doi: 10.1021/acsenergylett.6b00471

Song, T.-B., Yokoyama, T., Longsdon, J., Wasielewski, M. R., Aramaki, S., and Kanatzidis, M. G. (2018). Piperazine suppresses self-doping in CsSnI$_3$ perovskite solar cells. *ACS Appl. Energy Mater.* 1, 4221–4226. doi: 10.1021/acsaem.8b00866

Stoumpos, C. C., Malliakas, C. D., and Kanatzidis, M. G. (2013). Semiconducting tin and lead iodide perovskites with organic cations: phase transitions, high mobilities, and near-Infrared photoluminescent properties. *Inorg. Chem.* 52, 9019–9038. doi: 10.1021/ic401215x

Stoumpos, C. C., Mao, L., Malliakas, C. D., and Kanatzidis, M. G. (2016). Structure–band gap relationships in hexagonal polytypes and low-dimensional structures of hybrid tin iodide perovskites. *Inorg. Chem.* 56, 56–73. doi: 10.1021/acs.inorgchem.6b02764

Veronese, A., Patrini, M., Bajoni, D., Ciarrocchi, C., Quadrelli, P., and Malavasi, L. (2020). Highly tunable emission by halide engineering in lead-free perovskite-derivative nanocrystals: The Cs$_2$SnX$_6$ (X = Cl, Br, Br/I, I) system. *Front. Chem.* 8:35. doi: 10.3389/fchem.2020.00035

Wang, A., Yan, X., Zhang, M., Sun, S., Yang, M., Shen, W., et al. (2016). Controlled synthesis of lead-free and stable perovskite derivative Cs$_2$SnI$_6$ nanocrystals via a facile hot-injection process. *Chem. Mater.* 28, 8132–8140. doi: 10.1021/acs.chemmater.6b01329

Wang, X.-D., Huang, Y.-H., Liao, J.-F., Jiang, J., Zhou, L., Zhang, X.-Y., et al. (2019). *In situ* construction of a Cs$_2$SnI$_6$ perovskite nanocrystal/SnS$_2$ nanosheet heterojunction with boosted interfacial charge transfer. *J. Am. Chem. Soc.* 141, 13434–13441. doi: 10.1021/jacs.9b04482

Wang, Y., Tu, J., Li, T., Tao, C., Deng, X., and Li, Z. (2019). Convenient preparation of CsSnI$_3$ quantum dots, excellent stability, and the highest performance of lead-free inorganic perovskite solar cells so far. *J. Mater. Chem. A* 7, 7683–7690. doi: 10.1039/C8TA10901J

Wan-Jian, Y., Ji-Hui, Y., Kang, J., Yan, Y., and Wei, S.-H. (2015). Halide perovskite materials for solar cells: a theoretical review. *J. Mater. Chem. A* 3, 8926–8942. doi: 10.1039/C4TA05033A

Wijesekara, A., Varagnolo, S., Dabera, G. D. M. R., Marshall, K. P., Pereira, H. J., and Hatton, R. A. (2018). Assessing the suitability of copper thiocyanate as a hole-transport layer in inverted CsSnI$_3$ perovskite photovoltaics. *Sci. Rep.* 8:15722. doi: 10.1038/s41598-018-33987-7

Wu, C., Zhang, Q., Liu, Y., Luo, W., Guo, X., Huang, Z., et al. (2017). The dawn of lead-free perovskite solar cell: highly stable double perovskite Cs$_2$AgBiBr$_6$ film. *Adv. Sci.* 5:1700759. doi: 10.1002/advs.201700759

Wu, Y., Xie, F., Chen, H., Yang, H., Su, H., Cai, M., et al. (2017). Thermally stable MAPbI$_3$ perovskite solar cells with efficiency of 19.19% and area over 1cm^2 achieved by additive engineering. *Adv. Mater.* 29:1701073. doi: 10.1002/adma.201701073

Xiao, Z., Lei, H., Zhang, X., Zhou, Y., Hosono, H., and Kamiya, T. (2015). Ligand-hole in [SnI$_6$] unit and origin of band gap in photovoltaic perovskite variant Cs$_2$SnI$_6$. *Bull. Chem. Soc. Jpn.* 88, 1250–1255. doi: 10.1246/bcsj.20150110

Xiao, Z., Song, Z., and Yan, Y. (2019). From lead halide perovskites to lead-free metal halide perovskites and perovskite derivatives. *Adv. Mater.* 31:1803792. doi: 10.1002/adma.201803792

Xiao, Z., and Yan, Y. (2017). Progress in theoretical study of metal halide perovskite solar cell materials. *Adv. Energy Mater.* 7:1701136. doi: 10.1002/aenm.201701136

Yang, W. S., Park, B. W., Jung, E. H., Jeon, N. J., Kim, N. C., Lee, D. U., et al. (2017). Iodide management in formamidinium-lead-halide–based perovskite layers for efficient solar cells. *Science* 356, 1376–1379. doi: 10.1126/science.aan2301

Yin, H., Xian, Y., Zhang, Y., Li, W., and Fan, J. (2019). Structurally-stabilizing and friendly-environmental triggers: double-metallic lead-free perovskites. *Solar RRL* 3:1900148. doi: 10.1002/solr.201900148

Yuan, G., Huang, S., Qin, S., Wu, X., Ding, H., and Lu, A. (2019). Structural, optical and thermal properties of Cs$_2$SnI$_{6-x}$Br$_x$ mixed perovskite solid solution. *Eur. J. Inorg. Chem.* 20, 2524–2529. doi: 10.1002/ejic.201900120

Zhao, X.-G., Yang, D., Sun, Y., Li, T., Zhang, L., Yu, L., et al. (2017b). Cu–In halide perovskite solar absorbers. *J. Am. Chem. Soc.* 139, 6718–6725. doi: 10.1021/jacs.7b02120

Zhao, X.-G., Yang, J.-H., Fu, Y., Yang, D., Xu, Q., Yu, L., et al. (2017a). Design of lead-free inorganic halide perovskites for solar cells via cation-transmutation. *J. Am. Chem. Soc.* 139, 2630–2638. doi: 10.1021/jacs.6b09645

Zhu, W., Yao, T., Shen, Y., Xu, W., Gong, B., Wang, Y., et al. (2019). *In situ* investigation of water interaction with lead-free all inorganic perovskite (Cs$_2$SnI$_x$Cl$_{6-x}$). *J. Phys. Chem. C* 123, 14, 9575–9581. doi: 10.1021/acs.jpcc.9b00720

Zhu, Z., Li, N., Zhao, D., Wang, L., and Jen, A. K. Y. (2019). Improved efficiency and stability of Pb/Sn binary perovskite solar cells fabricated by galvanic displacement reaction. *Adv. Energy Mater.* 9:1802774. doi: 10.1002/aenm.201802774